Mathematics

AIMS Mathematics, 11(2): 4098–4122.
DOI: 10.3934/math.2026165
Received: 11 December 2025
Revised: 22 January 2026
Accepted: 30 January 2026
Published: 10 February 2026

https://www.aimspress.com/journal/Math

Research article

Electronic implementation of a new secure communication system based on the Lü hyperchaotic system

Fadia Zouad[1], Manal Messadi[2], Karim Kemih[2,*], Ahmad Taher Azar[3,4], Saim Ahmed[3,4,*] and Ahmed Redha Mahlous[3,4]

[1] Electronics Research Laboratory, University of 20 August 1955, Skikda, Algeria
[2] L2EI Laboratory, Mohamed Seddik Benyahia University, Jijel, Algeria
[3] College of Computer and Information Sciences, Prince Sultan University, Riyadh 11586, Saudi Arabia
[4] Automated Systems and Computing Lab (ASCL), Prince Sultan University, Riyadh, Saudi Arabia

* **Correspondence:** Email: k.kemih@gmail.com, sahmed@psu.edu.sa.

Abstract: This paper presents the design of a novel secure communication system based on the dynamics of the Lü hyperchaotic system. In the proposed scheme, the information signal is directly embedded into the hyperchaotic trajectories, ensuring a high level of data concealment. To achieve accurate synchronization between the transmitter and the receiver, a predictive control strategy combined with chaotic modulation is employed. This synchronization mechanism enables precise recovery of the embedded information signal. To evaluate the feasibility and robustness of the proposed cryptosystem, a dual validation framework is adopted. Numerical simulations are carried out using MATLAB/Simulink, and hardware-oriented simulations are performed using Multisim. The strong agreement between the numerical and circuit-level results confirms both the effectiveness and the reliability of the proposed approach. Overall, this work demonstrates the significant potential of hyperchaotic systems for secure communication applications.

Keywords: chaotic behavior; circuit implementation; predictive control; cryptosystem design
Mathematics Subject Classification: 34H10, 93C10, 93D05, 94A60

1. Introduction

The secure transmission of information has become a critical research topic in modern communication systems, particularly in applications requiring confidentiality, reliability, and resistance to unauthorized access. In recent years, chaotic systems have attracted significant interest due to their inherent complexity, broadband spectra, and extreme sensitivity to initial conditions. A fundamental contribution in this field was reported by Pecora and Carroll in 1990 [1], who demonstrated that two identical chaotic systems initialized with different initial conditions can achieve synchronization under appropriate coupling.

Chaotic synchronization ensures that the temporal evolution of a slave system follows the same dynamical behavior as that of a master system. Numerous synchronization techniques have been proposed in the literature, including passive and impulsive synchronization for a new four-dimensional chaotic system [2], observer-based synchronization of a new hybrid chaotic system [3], adaptive sliding-mode synchronization of second-order chaotic systems [4], and adaptive control strategies for new chaotic systems [5]. El Dessoky et al. [6] studied the control and function projective synchronization of a three-dimensional chaotic system by designing nonlinear control laws and proving stability using Lyapunov theory. Vaidyanathan and Azar [7] proposed a novel four-dimensional four-wing chaotic system with quadratic nonlinearities and achieved synchronization via an adaptive control scheme, supported by rigorous stability analysis and numerical simulations. Saadi et al. [8] developed an adaptive synergetic control approach for the synchronization of chaotic oscillator systems, effectively handling parameter uncertainties and guaranteeing asymptotic convergence of the synchronization errors. Additional synchronization approaches can be found in [9–11].

Synchronization plays a central role in secure communications, as it enables the receiver to accurately reconstruct the embedded information, thereby ensuring reliable transmission. Consequently, various secure communication schemes have been investigated. Representative examples include secure communication based on a Takagi–Sugeno fuzzy optimal time-varying disturbance observer combined with sliding-mode control [12], a communication scheme using a fractional-order delayed chaotic system with electronic circuit implementation [13], and a hybrid synchronization-based secure communication approach relying on minimal continuous chaos [14]. Despite these advances, achieving a trade-off between synchronization performance, security level, and implementation complexity remains a challenging issue.

Chaos-based encryption has also emerged as an effective approach for securing multimedia and networked data due to its strong randomness, sensitivity to initial conditions, and complex dynamical behavior. Recent studies exploit advanced chaotic systems, such as dual-memristor maps, hyperchaotic models, and neuron-inspired chaotic maps, to generate high-quality cryptographic keystreams with large key spaces and enhanced diffusion and confusion properties. To improve efficiency, selective encryption strategies and multilayer permutation-diffusion frameworks have been proposed, particularly for image and video data in resource-constrained environments. Gao et al. [15] propose a 3D memristive cubic chaotic map with dual discrete memristors, whose hardware implementation and experimental results demonstrate strong security performance and feasibility for real-time image encryption. In addition, the comprehensive review by Gao et al. [16] systematically analyzes recent chaos-based video encryption techniques, highlighting their effectiveness, implementation challenges, and robustness in practical multimedia security systems. Experimental and hardware validation results further confirm the practicality and robustness of chaos-based encryption schemes in various secure communication applications [17–19].

Among the different strategies used to enhance communication security and reliability, hyperchaotic systems stand out due to their higher level of complexity resulting from the presence of multiple positive Lyapunov exponents. Although hyperchaotic systems have been investigated in several works [20–22], their integration into secure communication frameworks combined with simple and efficient synchronization strategies remains relatively limited.

Motivated by these observations, this paper proposes a secure communication scheme based on the Lü hyperchaotic system. In the proposed approach, the information signal is embedded into the system dynamics using an inclusion-based modulation strategy, enhancing signal concealment. A predictive control algorithm is employed at the receiver side to achieve fast and robust synchronization, enabling accurate demodulation of the transmitted information. Furthermore, to bridge the gap between theoretical modeling and practical implementation, the effectiveness of the proposed scheme is validated through both numerical simulations using MATLAB/Simulink and circuit-level implementation using Multisim. This hardware-oriented validation enhances the practical relevance of the proposed secure communication system.

This work is organized as follows. Section 2 analyzes the Lü hyperchaotic system, focusing on its equilibrium points and stability. Section 3 presents the predictive control method. Section 4 introduces the scheme of the proposed hyperchaotic encryption system, detailing its components (the transmitter and receiver) and illustrating the synchronization performance through numerical simulations. Section 5 describes the electronic implementation of the encryption system and discusses the corresponding experimental results. Finally, Section 6 concludes this paper.

2. System description

Recently, by introducing a state-feedback controller into the classical Lü system, a new four-dimensional hyperchaotic system, referred to as the Lü hyperchaotic system, was proposed in [16]. The mathematical model of this system is given by:

$$\begin{cases} \dfrac{dx}{dt} = a\left(y - x\right) + w \\ \dfrac{dy}{dt} = cy - xz \\ \dfrac{dz}{dt} = xy - bz \\ \dfrac{dw}{dt} = xz + dw \end{cases}, \tag{2.1}$$

where x, y, z, and w are the state variables, and a, b, c, and d are real constant parameters. For the parameter values a=35, b=20, c=3, the dynamical behavior of the system varies according to the parameter d, as summarized below:

- when $1.03 < d < 0.46$, the system shows a periodic orbit;
- when $-0.46 < d \le -0.35$, the system exhibits periodic behavior;
- when $-0.35 < d < 1.30$, the system becomes hyperchaotic.

Figure 1 shows the hyperchaotic attractors of the Lü system for the parameter values a=35, b=20, c=3, and d=1.2, with the initial conditions (x(0),y(0),z(0),w(0))=(0.1,0.2,0.3,0.4). The complex and aperiodic trajectories observed in the phase space confirm the presence of hyperchaotic dynamics. To quantitatively evaluate the complexity of the Lü hyperchaotic system, the Lyapunov exponent spectrum is computed using the standard Wolf algorithm. The obtained Lyapunov exponents are shown in Figure 2. It can be observed that three Lyapunov exponents are positive ($\lambda_1 = 1.6665$, $\lambda_2 = 1.0494$, $\lambda_3 = 0.4479$, and $\lambda_4 = \text{-}22.0141$), which confirms the hyperchaotic nature of the system.

The presence of multiple positive Lyapunov exponents indicates strong sensitivity to initial conditions and enhanced dynamical complexity. These properties are highly desirable for secure communication applications, as they improve information masking and resistance to parameter estimation attacks.

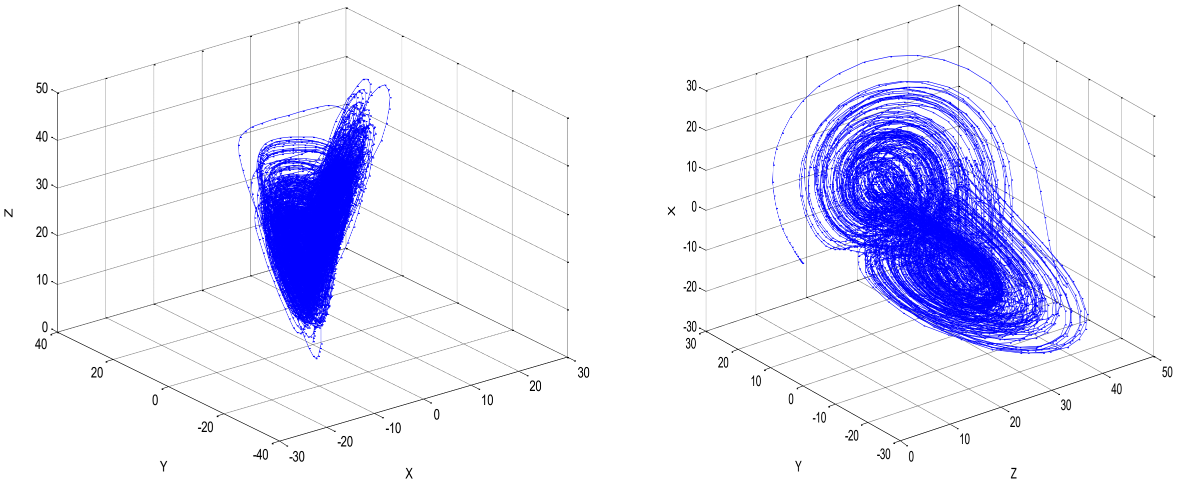

Figure 1. Hyperchaotic attractors of the Lü hyperchaotic system.

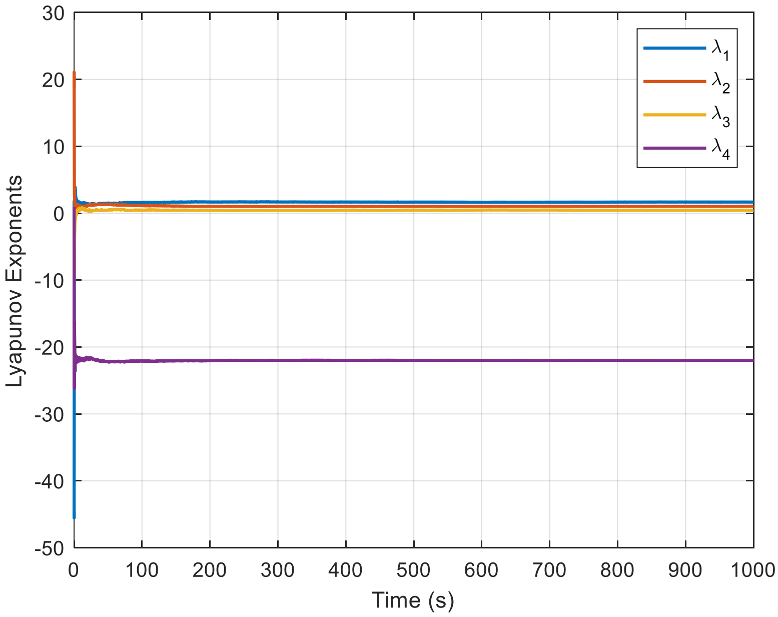

Figure 2. Lyapunov exponents of the hyperchaotic Lü system.

3. Theory of predictive control

In this section, the predictive control strategy used to synchronize the hyperchaotic transmitter and receiver systems is presented. Predictive control aims to suppress chaotic oscillations and force the system states to converge toward a desired equilibrium point by exploiting a one-step-ahead prediction of the system dynamics.

3.1. Problem formulation

Consider the nonlinear dynamical systems described by:

$$\dot{X}_m(t) = f\left(X_m(t)\right) + u(t), \tag{3.1}$$

where $X_m(t) \in \mathbb{R}^n$ denotes the state vector, $f(\cdot)$ is a continuous and differentiable nonlinear vector function, and $u(t)$ represents the control input. The objective of the predictive controller is to design the control input $u(t)$ such that the system state converges asymptotically to an unstable equilibrium point of the uncontrolled system.

3.2. Predictive control principle

Let x_e denote an equilibrium point of the uncontrolled system, which satisfies:

$$f(x_e) = 0. \tag{3.2}$$

The control input u is calculated based on the difference between the predicted state X_p and the current state X_m, according to the following relation [23,24]:

$$u = K\left(X_p - X_m\right). \tag{3.3}$$

The value of K must be calculated.

Based on the equilibrium point of the transmitter system, which is given by E,

$$\dot{X}_m = 0 \to E = f\left(E\right). \tag{3.4}$$

The approximation of the uncontrolled system is given by the following relation:

$$\delta\dot{X}_m = J\dot{X}_m, \tag{3.5}$$

where $\delta\dot{X}_m = \dot{X}_m - E$, and J is the Jacobian matrix of $f\left(X_m\right)$.

By applying a one-step ahead prediction of the uncontrolled state variable X_m (i.e., $X_p = \dot{X}_m$), the control law (3.3) is then rewritten as follows:

$$u = K\left(\dot{X}_m \text{-} X_m\right) = K\left(f\left(X_m\right) \text{-} X_m\right). \tag{3.6}$$

The system under control is expressed as follows:

$$\dot{X}_m = f(X_m) + K\left(f(X_m) - X_m\right). \tag{3.7}$$

The linearization around the unstable equilibrium point of the controlled drive system is given by the following relation:

$$\delta\dot{X}_m = J\delta X_m + K\left(J\delta X_m - \delta X_m\right) = \left(J + K\left(J - I\right)\right)\delta X_m, \tag{3.8}$$

where I is the identity matrix.

By choosing the Lyapunov function $V(x) = \delta X_m{}^T \delta X_m = \delta X_m{}^T I\,\delta X_m$, the system is globally asymptotically stable if there exists a constant $\alpha > 0$ such that:

$$\left(J + K\left(J - I\right)\right)^T + \left(J + K\left(J - I\right)\right) \le -\alpha I. \tag{3.9}$$

4. New cryptosystem based on the Lü hyperchaotic system

In this section, a new secure communication scheme based on the Lü hyperchaotic system is proposed. The objective is to embed the information signal into the hyperchaotic dynamics at the transmitter side and to recover it accurately at the receiver side through predictive synchronization and demodulation.

4.1. System architecture

Predictive control is employed to synchronize two identical Lü hyperchaotic systems initialized with different initial conditions. The information signal is embedded into the second state variable of the transmitter system. The overall structure of the proposed secure communication system is shown in Figure 3.

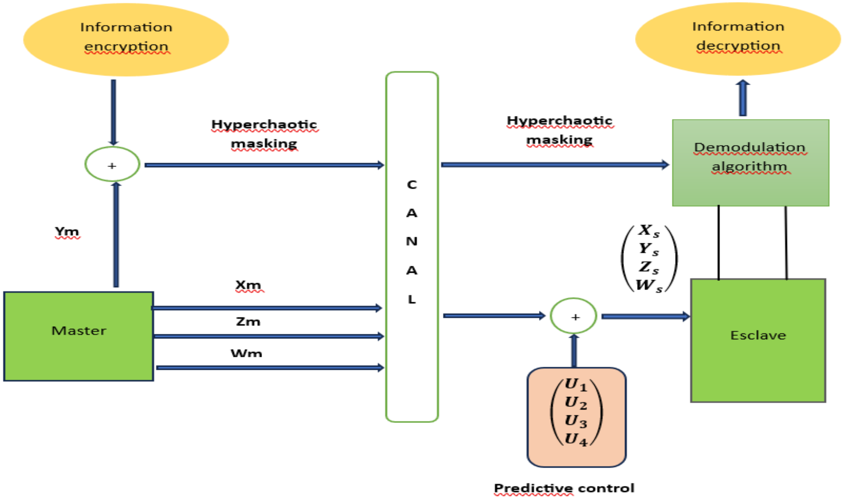

Figure 3. The secure system architecture.

4.2. The transmitter

The transmitter is described by the following set of equations:

$$\begin{cases} \dfrac{dx_m}{dt} = a\left(y_m - x_m\right) + w_m \\ \dfrac{dy_m}{dt} = cy_m - x_m z_m + \varsigma r \\ \dfrac{dz_m}{dt} = x_m y_m - bz_m \\ \dfrac{dw_m}{dt} = x_s z_s + dw_m \end{cases} \tag{4.1}$$

The transmitted information, denoted by $r(t)$ in Eq (4.1), is injected into the second state of the system, where ς is a positive constant. Using Simulink, the time evolutions of the system and its trajectory are plotted. The time evolution of the transmitter state variables in the presence of the information signal is shown in Figure 4. Figure 5 presents the corresponding strange attractor in the phase space. These figures demonstrate that the information signal is effectively concealed within the hyperchaotic dynamics. Despite the information injection, the system preserves its hyperchaotic behavior, which is essential for ensuring communication security. Even with the injected information, the system maintains its chaotic behavior. In the proposed scheme, the information signal is injected directly into the chaotic dynamics through a multiplicative coupling term. This approach fundamentally differs from classical chaos masking techniques, as the message actively modifies the system dynamics rather than being superimposed on a chaotic carrier. The coupling coefficient is treated as a secret key, further enhancing security. The security of the proposed communication scheme is based on the hyperchaotic dynamics of the Lü system and the synchronization-based information masking mechanism. The hyperchaotic system exhibits high sensitivity to initial conditions and parameters, making brute-force and parameter estimation attacks computationally infeasible. Spectral analysis attacks are mitigated by the broadband frequency characteristics of the hyperchaotic carrier, which effectively masks the message signal. Furthermore, return-map reconstruction attacks are hindered due to the high dimensionality and complexity of the hyperchaotic attractor. The embedding strength ζ plays a crucial role in balancing security and signal recovery performance. Larger values of ζ enhance synchronization accuracy and improve message recovery but may increase signal observability, whereas smaller values improve concealment at the expense of slower convergence. Simulation results confirm the existence of this trade-off, demonstrating that the appropriate selection of ζ ensures both security and reliable communication.

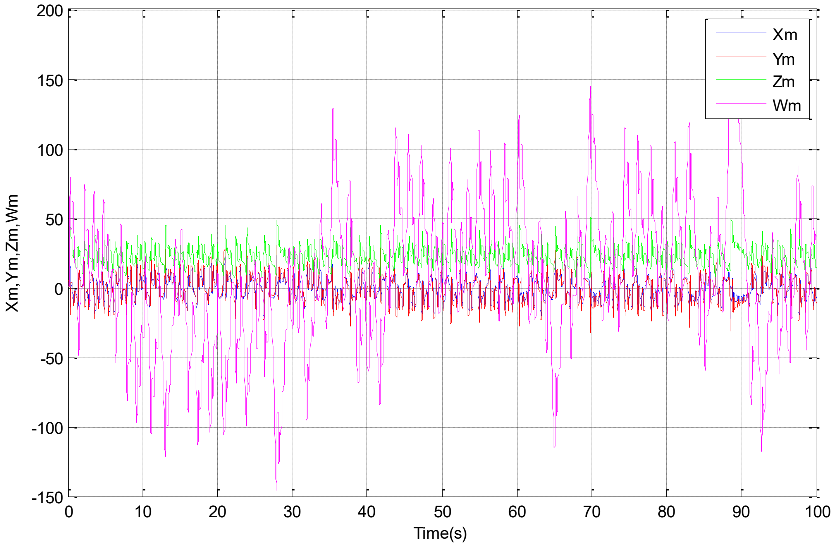

Figure 4. Time evolution of the four states of the Lü hyperchaotic system.

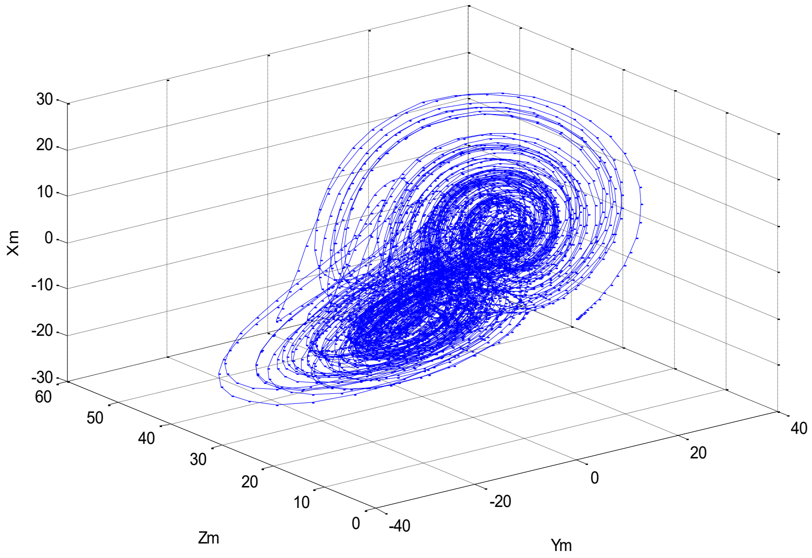

Figure 5. Strange attractor of the Lü hyperchaotic transmitter system in the x-y-z plane.

4.3. Receiver and demodulation scheme

The receiver system is composed of two subsystems. The first is a Lü hyperchaotic system, which includes the control input represented by the vector $\left|u_1 \quad u_2 \quad u_3 \quad u_4\right|^T$. This ensures synchronization with the transmitter.

The second subsystem is a demodulation algorithm. The demodulation strategy adopted in this work is inspired by the robust chaotic demodulation filter proposed by Wang and Wang [24]. An auxiliary variable $Q(t)$ is introduced to avoid direct differentiation of the transmitted signal, which is known to amplify noise. The variable $Q(t)$ acts as an internal reconstruction state that compensates for modeling uncertainties and synchronization imperfections. The recovered message is obtained as a linear combination of the synchronized chaotic state and the auxiliary variable. The parameter ζ represents the information embedding strength and plays a dual role: it ensures exponential convergence of the demodulation error while controlling the trade-off between recovery accuracy and security. A higher value of ζ accelerates convergence but may increase signal observability, whereas smaller values enhance concealment at the expense of slower convergence.

The two systems are described by the following equations:

$$\begin{cases} \dfrac{dx_s}{dt} = a\left(y_s - x_s\right) + w_{s?} + u \\ \dfrac{dy_s}{dt} = cy_s - x_s z_s + u_2 \\ \dfrac{dz_s}{dt} = x_s y_s - bz_s + u_3 \\ \dfrac{dw_s}{dt} = x_s z_s + dw_s + u_4 \end{cases} \tag{4.2}$$

$$\begin{cases} \dfrac{dQ}{dt} = -\zeta K\left[cy_m - x_m z_m + \zeta\hat{r}\left(t\right)\right] \\ \hat{r}\left(t\right) = \zeta K y_m\left(t\right) + Q \end{cases} \tag{4.3}$$

The variables $x_s, y_s, z_s, w_s \in R^n$ are the receiver states, K is a positive constant, and the $\hat{r}$ is the signal reconstructed using predictive control. Two gains are then calculated to ensure system synchronization.

The first gain corrects the error between the actual state of the system and the predicted state, thereby improving the accuracy of the control. The second gain is used to adjust the dynamics of the controller and mitigate the effects of hyperchaos, enhancing both the stability and robustness of the system's response.

The control input obtained is applied to the system's second and fourth states; its equation is given by:

$$\begin{aligned} u_1 &= 0 \\ u_2 &= k\left[c\left(y_s - y_m\right) - \left(x_s - x_m\right)\left(z_s - z_m\right) - \left(y_s - y_m\right)\right] \\ u_3 &= 0 \\ u_4 &= k\left[\left(x_s - x_m\right)\left(z_s - z_m\right) + d\left(w_s - w_m\right) - \left(w_s - w_m\right)\right] \end{aligned} \tag{4.4}$$

By inserting the equation into (4.2), the following expression is obtained:

$$\begin{cases} \dfrac{dx_s}{dt} = a\left(y_s - x_s\right) + w_s \\ \dfrac{dy_s}{dt} = cy_s - z_s + k\left[c\left(y_s - y_m\right) - \left(x_s - x_m\right)\left(z_s - z_m\right) - \left(y_s - y_m\right)\right] \\ \dfrac{dz_s}{dt} = x_s y_s - bz_s \\ \dfrac{dw_s}{dt} = x_s z_s + dw_s + k\left[\left(x_s - x_m\right)\left(z_s - z_m\right) + d\left(w_s - w_m\right) - \left(w_s - w_m\right)\right] \\ \begin{cases} \dfrac{dQ}{dt} = -\zeta K\left[cy_m - x_m z_m + \zeta \hat{r}\left(t\right)\right] \\ \hat{r}\left(t\right) = \zeta K y_m\left(t\right) + Q \end{cases} \end{cases} \tag{4.5}$$

The synchronization error between the transmitter and receiver is defined as:

$$\mathrm{e}\left(\mathrm{t}\right) = \begin{pmatrix} \mathrm{e_x} \\ \mathrm{e_y} \\ \mathrm{e_z} \\ \mathrm{e_w} \end{pmatrix} = \begin{pmatrix} x_s - x_m \\ y_s - y_m \\ z_s - z_m \\ w_s - w_m \end{pmatrix}. \tag{4.6}$$

The error dynamics equation for the synchronization between the transmitter and the receiver:

$$\begin{cases} \dot{e}_x = a\left(e_y - e_x\right) + e_w \\ \dot{e}_y = ce_y - e_x ez + x_s e_z + z_s e_x + K_y\left[ce_y - e_x e_z + x_s e_z + z_s e_x - e_y\right] \\ \dot{e}_z = exe_y - be_z + e_x y_s + x_s e_y \\ \dot{e}_w = e_x e_z + de_w - z_s e_x - x_s e_z + K_w\left[e_x e_z + de_w - z_s e_x - x_s e_z - e_w\right] \end{cases}, \tag{4.7}$$

where K_y and K_w are positive parameters to be determined.

By linearizing the nonlinear system (4.7) around the equilibrium x_f and using the first-order Taylor expansion of $f(x)$, we obtain:

$$\delta\dot{e}\left(t\right) = Df\left(x_f\right) A\delta e\left(t\right) + \delta u\left(t\right). \tag{4.8}$$

$Df\left(x_f\right)$ is the Jacobian matrix around the equilibrium point.

With the control law $u = K\left(\dot{e} - e\right)$ and in deviation coordinates about x_f (so that $x_{\text{ref}} =$ constant), the linearized closed loop is:

$$\delta\dot{e}\left(t\right) = A\delta e\left(t\right) + K\left(A\delta e\left(t\right) - \delta e\left(t\right)\right) = (A + KA - K)\delta e\left(t\right) = A_{ce}\delta e\left(t\right). \tag{4.9}$$

We consider the Lyapunov function:

$$V\left(x\left(t\right)\right) = e^T P e, \quad P = P^T > 0. \tag{4.10}$$

Its derivative along the trajectories of V is:

$$\dot{V}\left(x(t)\right) = \dot{e}^{T}(t)Pe(t) + e^{T}(t)P\dot{e}(t) = e^{T}(t)\left(A_{ce}^{T}P + PA_{ce}\right)e(t). \tag{4.11}$$

For asymptotic stability, $\dot{V}(x)$ must be negative definite. This requirement leads to the Lyapunov equation:

$$(A + AK - K)^{T}P + P(A + AK - K) = -O, \tag{4.12}$$

where $O = O^{T} > 0$ is a chosen positive definite matrix. Solving this equation for K guarantees that all trajectories converge to the origin.

For practical implementation, a diagonal structure of Kmay be assumed to simplify the solution. The feedback gains are determined by solving the linear matrix inequalities (LMIs) using MATLAB with the appropriate toolbox. The obtained result here is $K_w = -3$ and $K_y = -1.09$.

4.4. Synchronization error dynamics

Predictive synchronization is applied to the error system (4.7) by choosing the values of K according to the condition in (4.13). The initial conditions of the drive and response systems are ($x_m(0)y_m(0)z_m(0)w_m(0)$) = (0.1, 0.2, 0.3, 0.4) ^{T} and ($x_s(0)y_s(0)z_s(0)w_s(0)$)^{T} = (1, 2, 3, 4), respectively.

To further validate the effectiveness of the proposed approach, a comparison with a classical backstepping control strategy has been included, as illustrated in Figure 6. Both controllers are applied to the same controller–target Lü hyperchaotic systems, using identical system parameters and intentionally distant initial conditions to demonstrate global synchronization capability. Figure 7 presents the synchronization error dynamics for both approaches. The predictive controller achieves faster convergence with a time of 2.77s, compared to 6.78s obtained using the backstepping controller. Moreover, the steady-state mean squared error (MSE) is reduced from 1.33 × 10^{-5} (backstepping) to 1.61 × 10^{-7} (predictive control), demonstrating a significant improvement in synchronization accuracy. These results confirm that the proposed predictive control strategy outperforms the backstepping method in terms of convergence speed and steady-state synchronization precision.

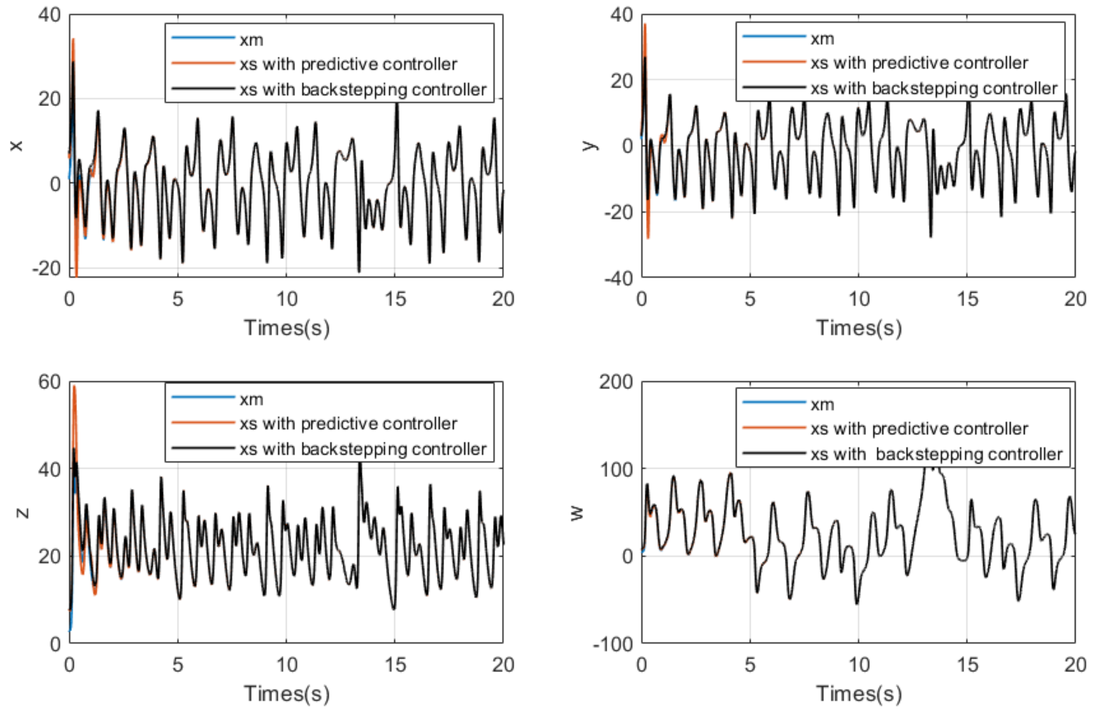

Figure 6. Synchronization performance under predictive and backstepping controllers.

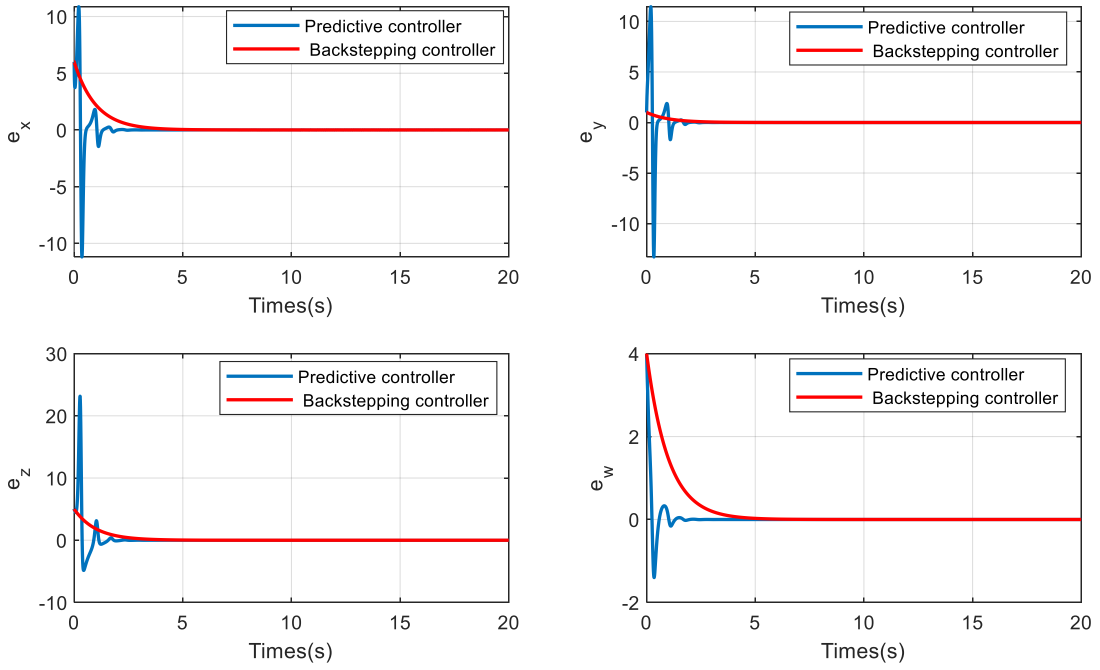

Figure 7. Synchronization error comparison between the predictive control approach and the backstepping controller.

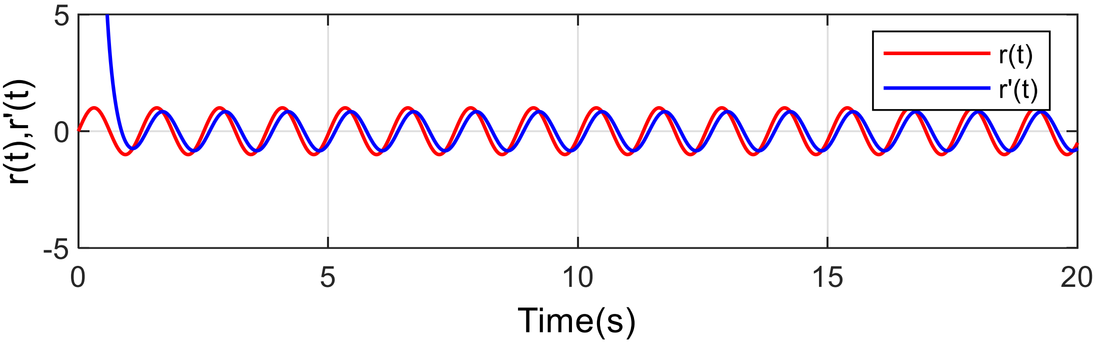

Figure 8. Comparison between the transmitted and recovered signal.

Figure 8 shows the transmitted information signal and the corresponding recovered signal at the receiver side. It can be clearly observed that the two signals are almost identical, with negligible distortion and time delay. This result confirms the effectiveness of the proposed synchronization and demodulation scheme and demonstrates the accurate recovery of the transmitted information.

5. Implementation of the cryptosystem

The electronic circuits presented in this work are implemented and validated using Multisim simulations, which provide a hardware-oriented environment for evaluating the feasibility of the proposed secure communication system. Each circuit block is designed using commercially available components. In practical implementations, component tolerances, thermal noise, and power supply fluctuations may introduce deviations from ideal behavior. These nonideal factors can affect signal amplitude and synchronization accuracy. However, chaotic synchronization is known to exhibit a certain degree of robustness against such perturbations, allowing the proposed system to maintain stable operation within reasonable tolerance ranges.

It should be noted that the present study focuses on simulation-based validation. The design and experimental testing of a physical prototype, including detailed noise characterization and tolerance analysis, are considered important future research directions.

5.1. Transmitter circuit implementation

To implement the emitter's equations, several operational amplifiers, including LM741CN, the analog multiplier AD633 with ± 15V, some resistors, and some capacitors are used to perform additions and subtractions.

The transmitter hyperchaotic system is given by Eq (4.1). In order to implement this system using analog electronic components, each state variable is mapped to a corresponding voltage signal. The time derivatives are realized through ideal RC integrators. For an integrator composed of a resistor R and a capacitor C, the relationship between the input and output voltages is expressed as $V_{\text{out}}(t) = -\frac{1}{RC}\int V_{\text{in}}(t)\,dt \Rightarrow \frac{dV_{\text{out}}(t)}{dt} = -\frac{1}{RC}V_{\text{in}}(t)$.

The first state equation is implemented by a summing amplifier followed by an integrator. Using the integrator with R_6 and C_1, the voltage $x_m(t)$ is given by $x_m(t)=-\frac{R_6}{C_1R_2}\left(\frac{y_m}{R_1}-\frac{x_m}{R_3}+\frac{w_m}{R_{11}}\right)$. The parameter a is selected through the resistor ratios: $a=\frac{R_6}{C_1R_2R_1}=-\frac{R_6}{C_1R_2R_3}$. The nonlinear term x_my_m is generated by an analog multiplier. After summation and integration with R_7 and C_1, the voltage $y_m(t)$ becomes: $y_m(t)=\frac{R_7}{C_1R_4}\left(\frac{x_my_m}{R_9}+\frac{y_m}{R_{10}}+\frac{r(t)}{R_{65}}\right)$. Similarly, the state equation for z_m is implemented using a multiplier and an integrator, $z_m(t)=\frac{R_8}{C_3R_5}\left(\frac{x_my_m}{R_{13}}-\frac{z_m}{R_{12}}\right)$. The product x_mz_m is realized using a multiplier and then integrated as follows $w_m(t)=\frac{R_{17}}{C_4R_{16}}\left(\frac{x_mz_m}{R_9}-\frac{w_m}{R_{14}}\right)$.

In summary, the hyperchaotic system (4.1) can be expressed as follows:

$$\begin{cases} x_m(t)=\left[-\frac{R_6}{C_1R_2}\left(\frac{y_m}{R_1}-\frac{x_m}{R_3}+\frac{w_m}{R_{11}}\right)\right] \\ y_m(t)=\left[\frac{R_7}{C_1R_4}\left(\frac{x_my_m}{R_9}+\frac{y_m}{R_{10}}+\frac{r(t)}{R_{65}}\right)\right] \\ z_m(t)=\left[\frac{R_8}{C_3R_5}\left(\frac{x_my_m}{R_{13}}-\frac{z_m}{R_{12}}\right)\right] \\ w_m(t)=\left[\frac{R_{17}}{C_4R_{16}}\left(\frac{x_mz_m}{R_9}-\frac{w_m}{R_{14}}\right)\right] \end{cases} \tag{5.1}$$

The resistor and capacitor values in Eq (5.1) are defined as follows:
Resistors:

- $R_1 = R_3 = 27.77$ kΩ
- $R_2 = R_4 = R_5 = R_6 = R_7 = R_8 = R_{16} = R_{17} = 100$ kΩ
- $R_{13} = 333.333$ kΩ
- $R_{14} = 12{,}000$ kΩ
- $R_{11} = 1$ MΩ
- $R_{15} = R_{13} = R_9 = R_{65} = 100$ kΩ
- $R_{10} = 50$ kΩ

Capacitors:

- $C_1 = C_2 = C_3 = C_4 = 0.1\ \mu$F

Figure 9 presents the complete electronic circuit of the Lü hyperchaotic transmitter implemented in Multisim. The circuit directly realizes the mathematical model described in Eq (5.1), where each state variable is mapped to an analog voltage signal, and the corresponding differential equations are implemented using operational amplifiers, RC integrators, and analog multipliers. This figure confirms the practical realizability of the theoretical hyperchaotic model.

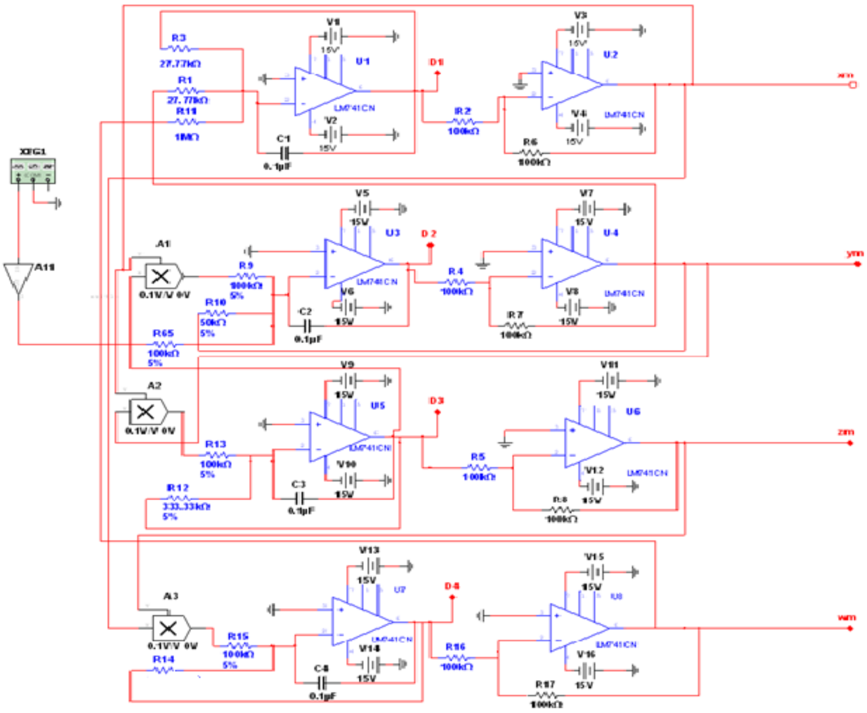

Figure 9. Electronic circuit of the transmitter.

Figures 10–13 show the time evolution of the transmitter state variables. By comparing these results with those presented in Figure 4, it can be observed that identical dynamical behaviors are obtained, confirming the consistency between the two sets of results.

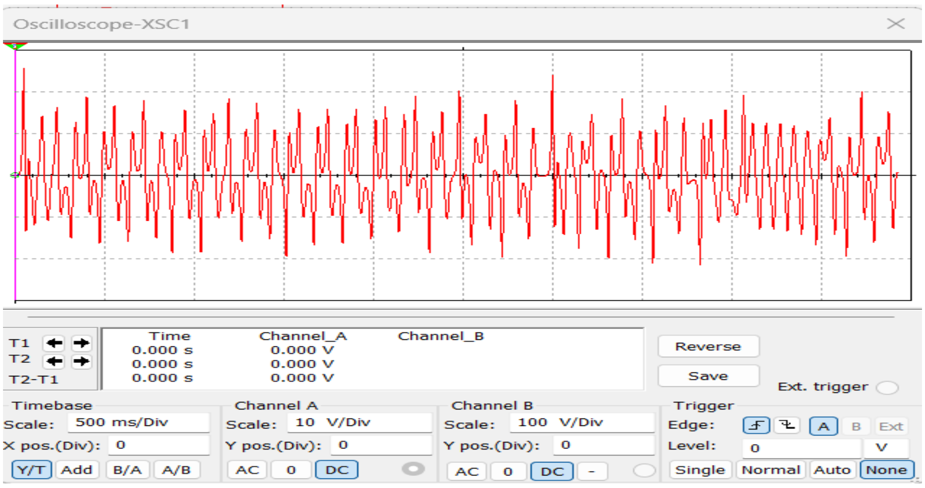
Oscilloscope-XSC1

	Time	Channel_A	Channel_B
T1	0.000 s	0.000 V	
T2	0.000 s	0.000 V	
T2-T1	0.000 s	0.000 V	

Timebase
Scale: 500 ms/Div
X pos.(Div): 0

Channel A
Scale: 10 V/Div
Y pos.(Div): 0

Channel B
Scale: 100 V/Div
Y pos.(Div): 0

Trigger
Edge:
Level: 0 V

Figure 10. Trajectory of the transmitter state xm.

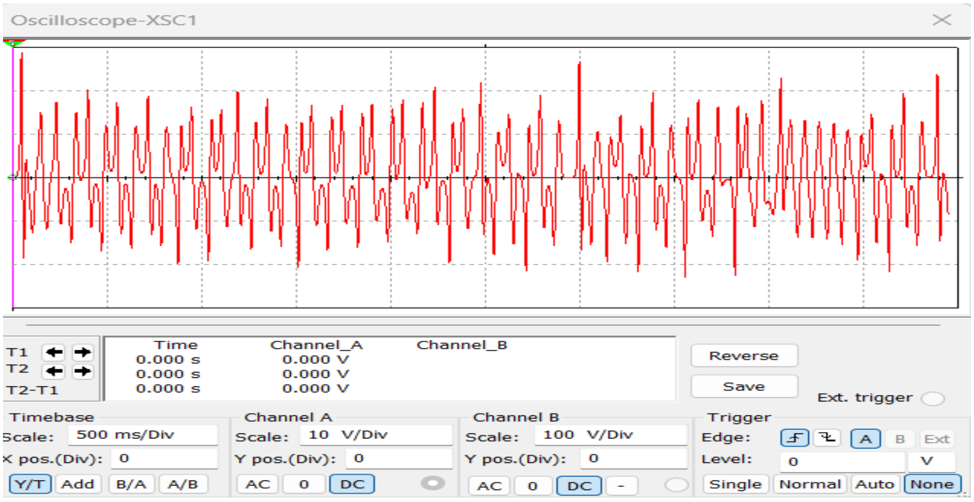

	Time	Channel_A	Channel_B
T1	0.000 s	0.000 V	
T2	0.000 s	0.000 V	
T2-T1	0.000 s	0.000 V	

Timebase Scale: 500 ms/Div X pos.(Div): 0
Channel A Scale: 10 V/Div Y pos.(Div): 0
Channel B Scale: 100 V/Div Y pos.(Div): 0
Trigger Edge: Level: 0 V

Figure 11. Trajectory of the transmitter state ym.

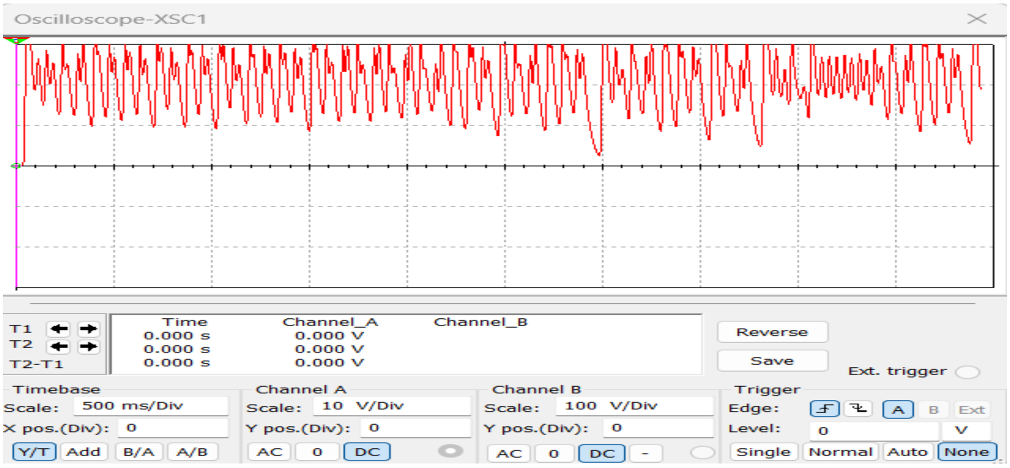

	Time	Channel_A	Channel_B
T1	0.000 s	0.000 V	
T2	0.000 s	0.000 V	
T2-T1	0.000 s	0.000 V	

Timebase Scale: 500 ms/Div X pos.(Div): 0
Channel A Scale: 10 V/Div Y pos.(Div): 0
Channel B Scale: 100 V/Div Y pos.(Div): 0
Trigger Edge: Level: 0 V

Figure 12. Trajectory of the transmitter state zm.

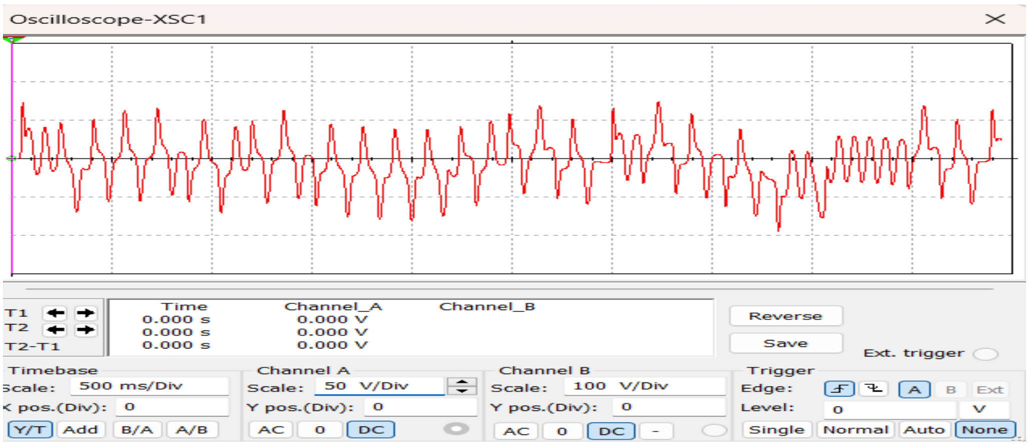

	Time	Channel_A	Channel_B
T1	0.000 s	0.000 V	
T2	0.000 s	0.000 V	
T2-T1	0.000 s	0.000 V	

Timebase Scale: 500 ms/Div X pos.(Div): 0
Channel A Scale: 50 V/Div Y pos.(Div): 0
Channel B Scale: 100 V/Div Y pos.(Div): 0
Trigger Edge: Level: 0 V

Figure 13. Trajectory of the transmitter state wm.

5.2. Receiver circuit implementation

Similar to the transmitter design, a circuit will be developed for the receiver. The following figure illustrates the corresponding equations, and the controller circuit will be integrated through its various outputs:

$$\begin{cases} x_s(t)=\left[-\dfrac{R_{20}}{C_7R_{27}}\left(\dfrac{y_s}{R_{18}}-\dfrac{x_s}{R_{19}}+\dfrac{w_s}{R_{34}}+U_1\right)\right] \\ y_s(t)=\left[\dfrac{R_{21}}{C_5R_4}\left(\dfrac{x_sy_s}{R_{23}}+\dfrac{y_s}{R_{24}}+\dfrac{U_2}{R_{63}}\right)\right] \\ z_s(t)=\left[\dfrac{R_{28}}{C_6R_{29}}\left(\dfrac{x_sy_s}{R_{26}}-\dfrac{z_s}{R_{25}}+U_3\right)\right] \\ w_s(t)=\left[\dfrac{R_{32}}{C_8R_{33}}\left(\dfrac{x_sz_s}{R_{31}}-\dfrac{w_s}{R_{30}}+\dfrac{U_4}{R_{64}}\right)\right] \end{cases} \tag{5.2}$$

The resistor and capacitor values in the Eq (5.2) are defined as follows:

Resistors:

- $R_{18} = R_{19} = 27.77\ \text{k}\Omega$
- $R_{34} = 1\ \text{M}\Omega$
- $R_{24} = 50\ \text{k}\Omega$
- $R_{64} = 1000\ \text{k}\Omega$
- $R_{20} = R_{21} = R_{22} = R_{23} = R_{26} = R_{27} = R_{28} = R_{29} = R_{31} = R_{32} = R_{33} = 100\ \text{k}\Omega$
- $R_{25} = 333.333\ \text{k}\Omega$
- $R_{30} = 120{,}000\ \text{k}\Omega$
- $R_{63} = 100\ \text{k}\Omega$

Capacitors:

- $C_5 = C_6 = C_7 = C_8 = 0.1\ \mu\text{F}$

Figure 14 presents the electronic circuit of the receiver subsystem incorporating the predictive control structure. This circuit implements the synchronization equations derived in Section 4 and provides a hardware-oriented realization of the theoretical receiver model.

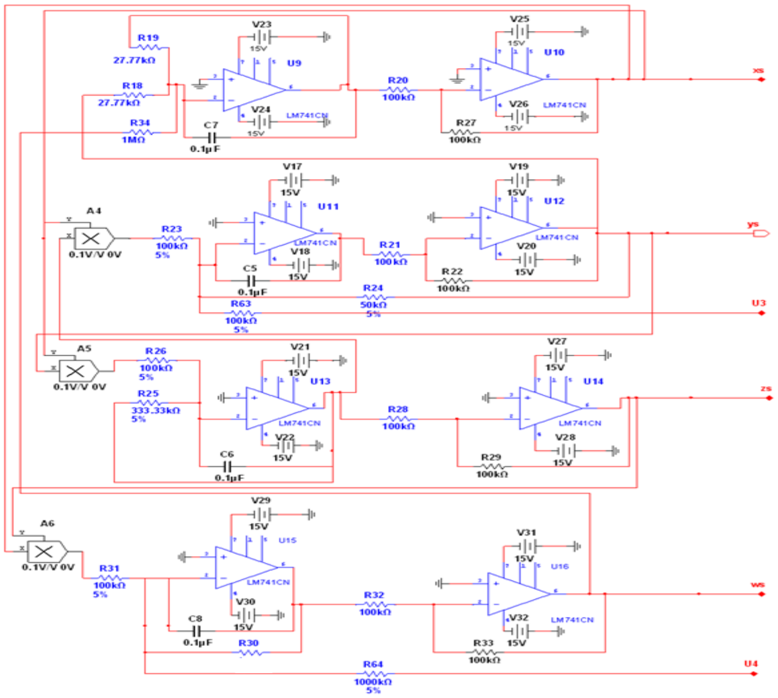

Figure 14. Electronic circuit of the receiver.

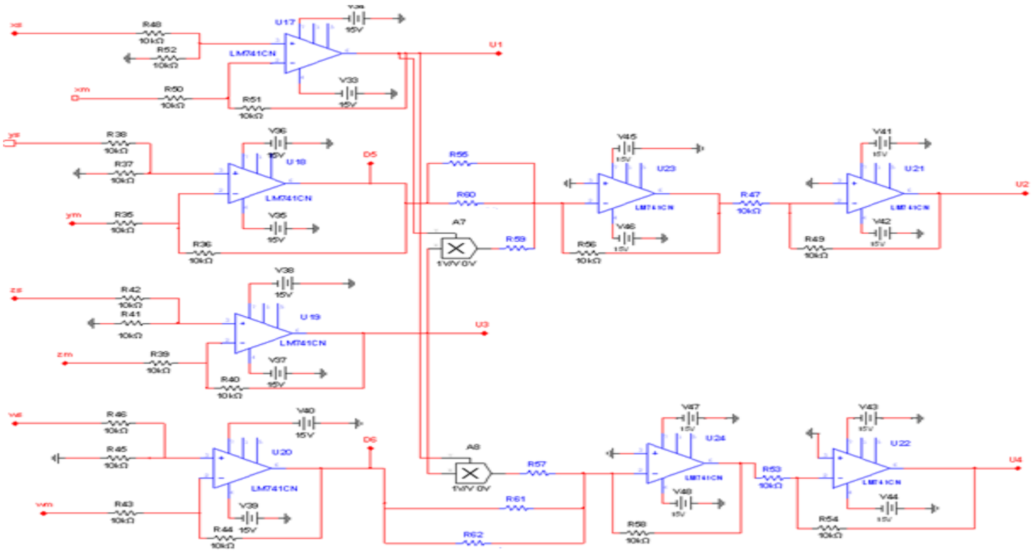

Figure 15. Secure communication control circuit.

Figure 15 shows the complete secure communication control circuit, integrating the transmitter, receiver, and control subsystems. This figure highlights the overall system architecture and illustrates how synchronization and demodulation are achieved within a unified electronic framework.

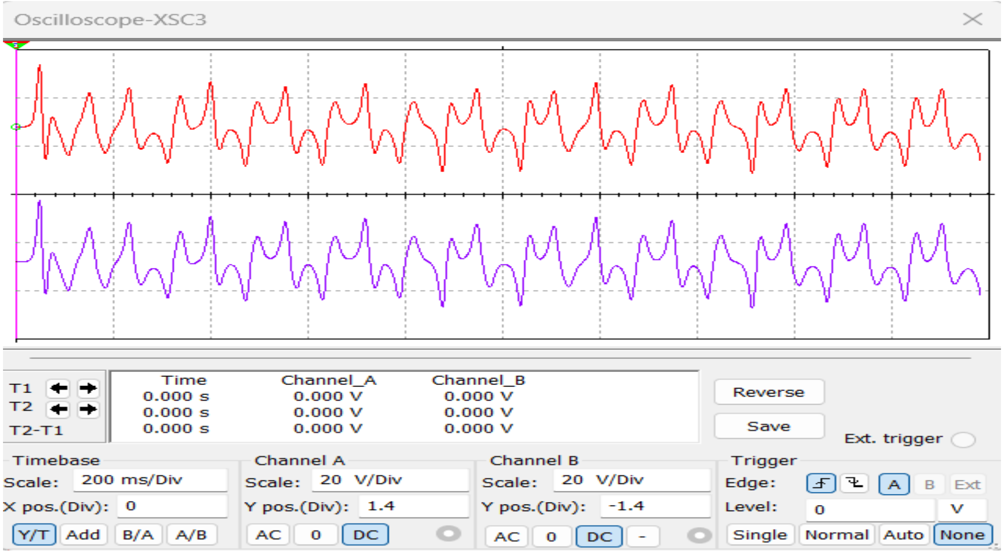

Oscilloscope-XSC3

```
         Time      Channel_A   Channel_B
T1       0.000 s   0.000 V     0.000 V
T2       0.000 s   0.000 V     0.000 V
T2-T1    0.000 s   0.000 V     0.000 V
```

Timebase Scale: 200 ms/Div; X pos.(Div): 0

Channel A Scale: 20 V/Div; Y pos.(Div): 1.4

Channel B Scale: 20 V/Div; Y pos.(Div): -1.4

Trigger Level: 0 V

Figure 16. Synchronization of states x_m and x_s simulated in Multisim.

Figure 16 illustrates the synchronization between the transmitter and receiver states x_m and x_s. The convergence of both trajectories demonstrates the effectiveness of the predictive control strategy and validates the theoretical synchronization conditions derived in Section 4.

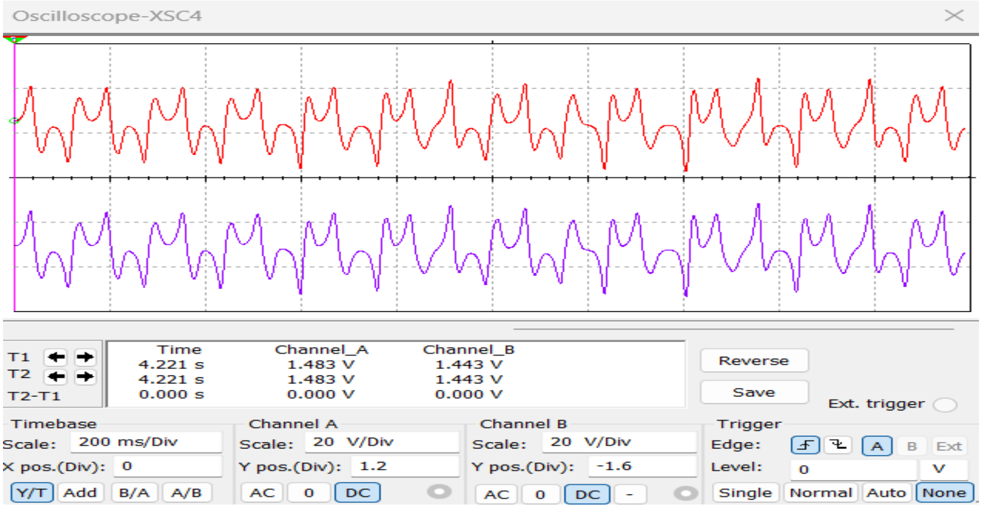

Oscilloscope-XSC4

```
         Time      Channel_A   Channel_B
T1       4.221 s   1.483 V     1.443 V
T2       4.221 s   1.483 V     1.443 V
T2-T1    0.000 s   0.000 V     0.000 V
```

Timebase Scale: 200 ms/Div; X pos.(Div): 0

Channel A Scale: 20 V/Div; Y pos.(Div): 1.2

Channel B Scale: 20 V/Div; Y pos.(Div): -1.6

Trigger Level: 0 V

Figure 17. Synchronization of states y_m and y_s simulated in Multisim.

Figure 17 presents the synchronization performance of the states y_m and y_s. The rapid convergence and negligible steady-state error indicate the robustness of the proposed control scheme against mismatched initial conditions.

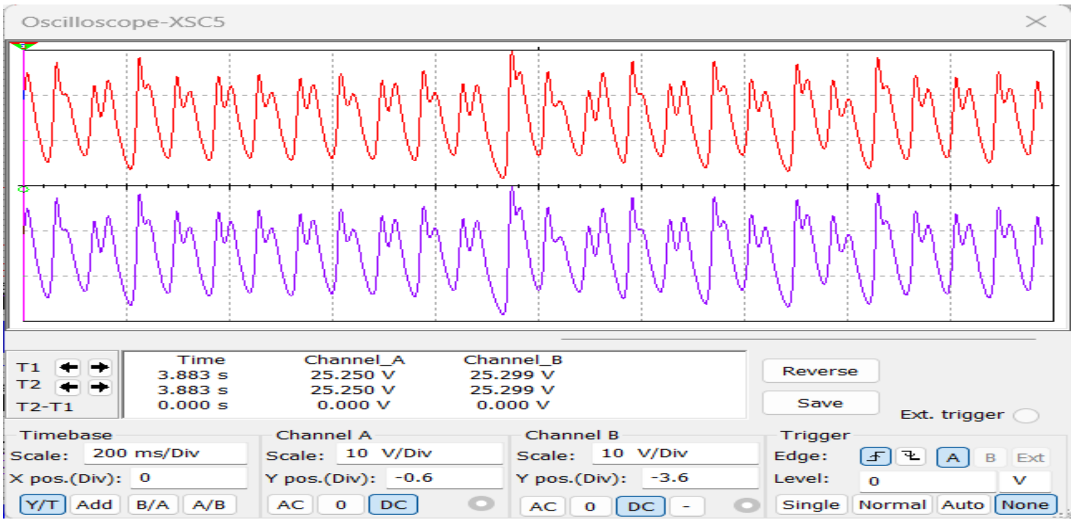

	Time	Channel_A	Channel_B
T1	3.883 s	25.250 V	25.299 V
T2	3.883 s	25.250 V	25.299 V
T2-T1	0.000 s	0.000 V	0.000 V

Timebase
Scale: 200 ms/Div
X pos.(Div): 0

Channel A
Scale: 10 V/Div
Y pos.(Div): -0.6

Channel B
Scale: 10 V/Div
Y pos.(Div): -3.6

Trigger
Edge:
Level: 0 V

Figure 18. Synchronization of states zm and zs simulated in Multisim.

Figure 18 shows the synchronization behavior of the states z_m and z_s. This result further confirms that the predictive controller ensures global synchronization of all hyperchaotic states, in agreement with the Lyapunov-based stability analysis.

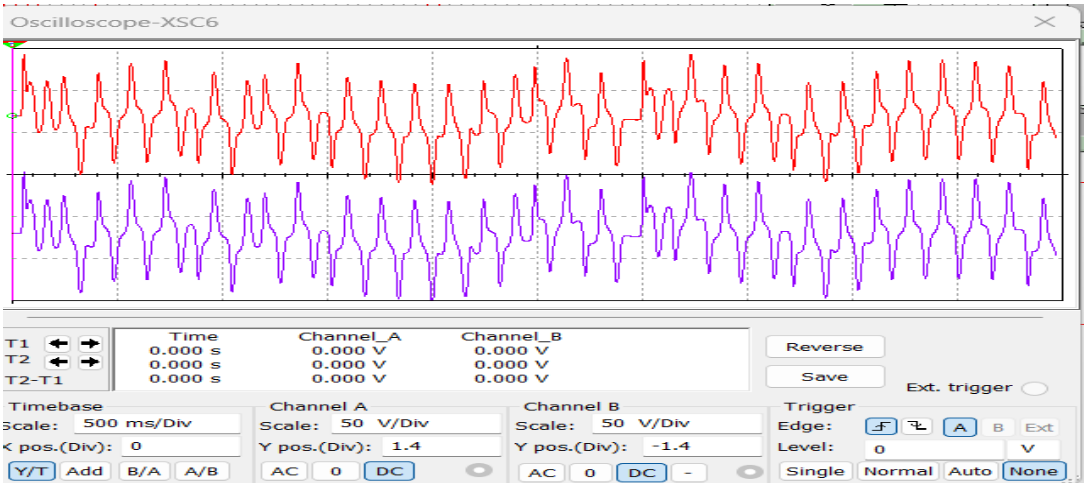

	Time	Channel_A	Channel_B
T1	0.000 s	0.000 V	0.000 V
T2	0.000 s	0.000 V	0.000 V
T2-T1	0.000 s	0.000 V	0.000 V

Timebase
Scale: 500 ms/Div
X pos.(Div): 0

Channel A
Scale: 50 V/Div
Y pos.(Div): 1.4

Channel B
Scale: 50 V/Div
Y pos.(Div): -1.4

Trigger
Edge:
Level: 0 V

Figure 19. Synchronization of states wm and ws simulated in Multisim.

Figure 19 shows the synchronization between the transmitter and receiver states w_m and w_s. The strong overlap of the two signals confirms the achievement of complete state synchronization. These results are fully consistent with, and further validate, the synchronization performance previously demonstrated in Figure 6, which is essential for reliable information recovery.

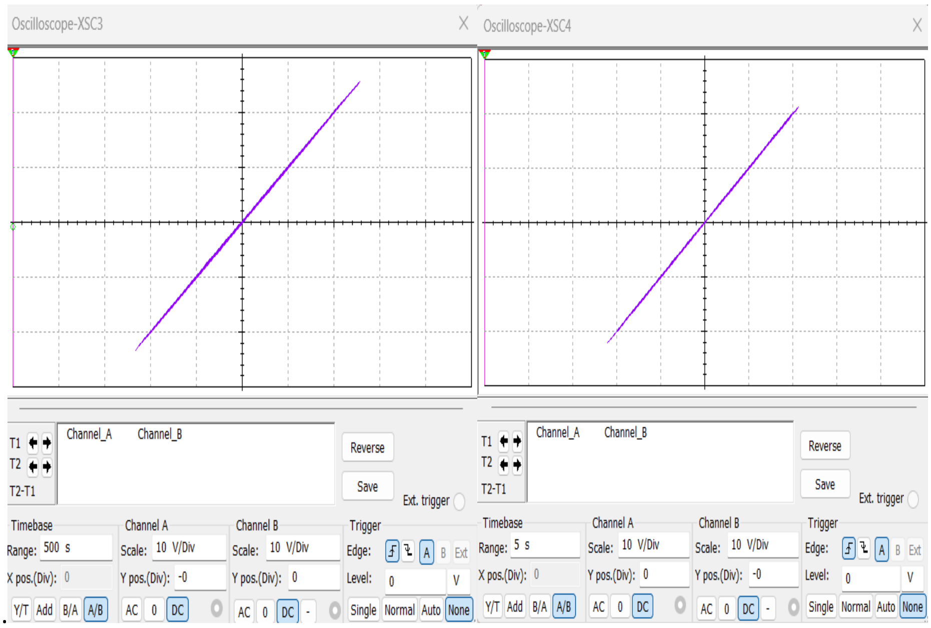

Oscilloscope-XSC3: Timebase Range: 500 s; X pos.(Div): 0; Channel A Scale: 10 V/Div; Y pos.(Div): -0; Channel B Scale: 10 V/Div; Y pos.(Div): 0; Trigger Level: 0 V

Oscilloscope-XSC4: Timebase Range: 5 s; X pos.(Div): 0; Channel A Scale: 10 V/Div; Y pos.(Div): 0; Channel B Scale: 10 V/Div; Y pos.(Div): -0; Trigger Level: 0 V

Figure 20. Evolution of state x_m as a function of state x_s and y_m as a function of state y_s.

Figures 20 and 21 illustrate the phase-space relationships between the corresponding transmitter and receiver states. Figure 20 shows the evolution of $x_m$versus x_s and y_m versus y_s, where the diagonal alignment of the trajectories provides a clear geometric confirmation of perfect synchronization, complementing the time-domain results presented in Figures 16 and 17. Figure 21 depicts the phase-space relationships between z_m and z_s, as well as between w_m and w_s, where the convergence of the trajectories onto the synchronization manifold further confirms the consistency between theoretical predictions and circuit-level simulation results.

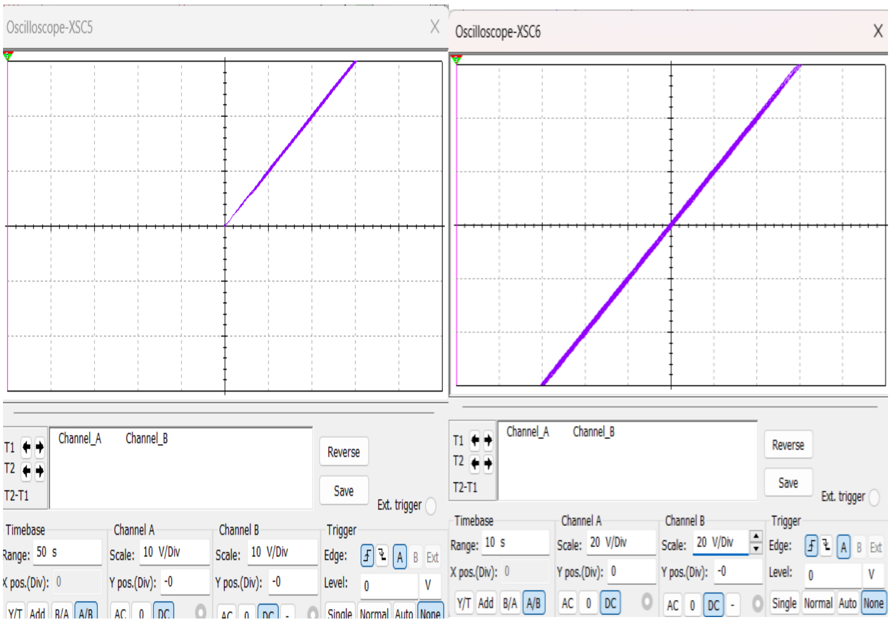

Oscilloscope-XSC5: Timebase Range: 50 s; X pos.(Div): 0; Channel A Scale: 10 V/Div; Y pos.(Div): -0; Channel B Scale: 10 V/Div; Y pos.(Div): -0; Trigger Level: 0 V

Oscilloscope-XSC6: Timebase Range: 10 s; X pos.(Div): 0; Channel A Scale: 20 V/Div; Y pos.(Div): 0; Channel B Scale: 20 V/Div; Y pos.(Div): -0; Trigger Level: 0 V

Figure 21. Evolution of state z_m as a function of state z_s and w_m as a function of state w_m.

5.3. Demodulation circuit implementation

Figure 22 illustrates the electronic circuit employed for chaotic signal demodulation at the receiver side. This circuit implements the demodulation algorithm defined in Eq (4.3), enabling robust reconstruction of the embedded information while avoiding direct differentiation of the chaotic signal. Figure 23 compares the transmitted information signal with the recovered signal obtained after synchronization and demodulation. Compared with the results shown in Figure 9, a strong agreement is observed between the two signals, demonstrating the effectiveness of the proposed secure communication scheme and confirming the consistency among the theoretical analysis, numerical simulations, and experimental implementation.

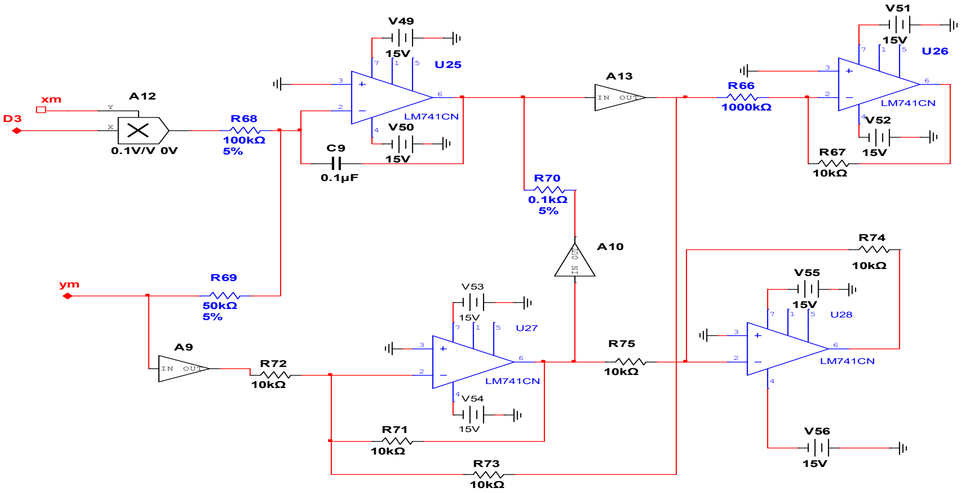

Figure 22. Electronic circuit for signal demodulation.

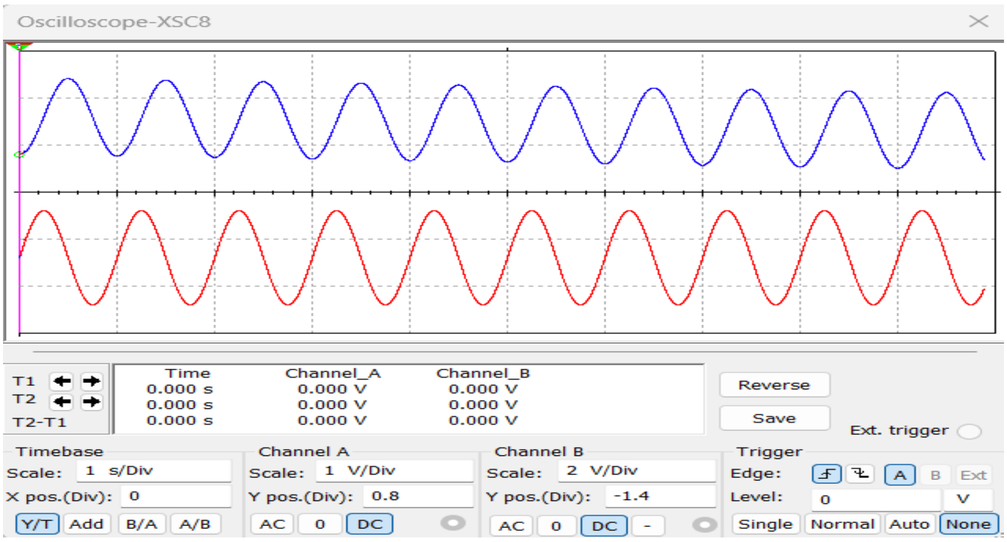
Oscilloscope-XSC8

	Time	Channel_A	Channel_B
T1	0.000 s	0.000 V	0.000 V
T2	0.000 s	0.000 V	0.000 V
T2-T1	0.000 s	0.000 V	0.000 V

Reverse

Save

Ext. trigger

Timebase
Scale: 1 s/Div
X pos.(Div): 0
Y/T Add B/A A/B

Channel A
Scale: 1 V/Div
Y pos.(Div): 0.8
AC 0 DC

Channel B
Scale: 2 V/Div
Y pos.(Div): -1.4
AC 0 DC -

Trigger
Edge: A B Ext
Level: 0 V
Single Normal Auto None

Figure 23. Transmitted signal and recovered signal.

6. Conclusions

In this paper, a secure communication scheme based on a four-dimensional Lü hyperchaotic system synchronized via predictive control has been presented. The proposed approach enables reliable synchronization between the transmitter and receiver and allows accurate recovery of the embedded information signal. The effectiveness of the scheme has been validated through numerical simulations using MATLAB/Simulink, as well as circuit-level implementation using Multisim. A comparative analysis with a classical backstepping synchronization controller demonstrates that the proposed predictive control strategy achieves faster convergence and lower steady-state synchronization error, highlighting its superiority in terms of efficiency and performance. The current study is limited to simulation-based validation, and the use of a sinusoidal information signal does not fully reflect the complexity of real-world communication scenarios. Furthermore, nonideal effects in physical hardware have not been experimentally verified. Future work will aim at the development of a real-time hardware prototype to experimentally validate the proposed scheme. While the present study deliberately focuses on single-state information embedding to ensure conceptual clarity and practical hardware feasibility, the proposed framework is inherently flexible and can be extended to multistate or multichannel embedding strategies. In such extensions, the information signal may be injected into multiple state equations or distributed among parallel chaotic subsystems, which could further improve both security performance and data throughput. These extensions constitute promising directions for future research.

Author contributions

Fadia Zouad: Conceptualization, methodology, investigation, writing-original draft preparation; Manal Messadi: Supervision, methodology, formal analysis, validation; Karim Kemih: Supervision, formal analysis, software development, visualization, writing-review and editing; Ahmad Taher Azar: Conceptualization, validation, resources, verification, writing-review, funding acquisition; Saim Ahmed: Verification, writing-review and editing; Ahmed Redha Mahlous: Investigation, methodology. All authors have read and approved the final version of the manuscript for publication.

Use of Generative-AI tools declaration

The authors declare that they have not used any artificial intelligence (AI) tools in creating this article.

Acknowledgments

This paper is derived from a research grant funded by the Research, Development, and Innovation Authority (RDIA), Kingdom of Saudi Arabia, with grant number 13382-psu-2023-PSNU-R-3-1-EI-. The authors would like to acknowledge Prince Sultan University, Riyadh, Saudi Arabia for their support of this publication. This research is supported by the Automated Systems and Computing Lab (ASCL), Prince Sultan University, Riyadh, Saudi Arabia.

Conflict of interest

The authors declare that they have no interests in this paper.

References

1. L. M. Pecora, T. L. Carroll, Synchronization in chaotic systems, *Phys. Rev. Lett.*, **64** (1990), 821–824. https://doi.org/10.1103/PhysRevLett.64.821
2. H. Hamiche, K. Kemih, M. Ghanes, G. Zhang, S. Djennoune, Passive and impulsive synchronization of a new four-dimensional chaotic system, *Nonlinear Anal.-Theor.*, **74** (2011), 1146–1154. https://doi.org/10.1016/j.na.2010.09.051
3. H. Bouraoui, K. Kemih, Observer based synchronization of a new hybrid chaotic system and its application to secure communications, *Acta Phys. Pol. A*, **123** (2013), 259–262. https://doi.org/10.12693/APhysPolA.123.259
4. Q. J. Yao, Synchronization of second order chaotic systems with uncertainties and disturbances using fixed-time adaptive sliding mode control, *Chaos Soliton. Fract.*, **142** (2021), 110372. https://doi.org/10.1016/j.chaos.2020.110372
5. A. Roldán-Caballero, J. H. Pérez-Cruz, E. Hernández-Márquez, J. R. García-Sánchez, M. Ponce-Silva, J. D. J. Rubio, et al., Synchronization of a new chaotic system using adaptive control: design and experimental implementation, *Complexity*, **2023** (2023), 2881192. https://doi.org/10.1155/2023/2881192
6. M. M. El Dessoky, E. Alzahrani, Z. A. Abdulmannan, Control and function projective synchronization of 3D chaotic system, *Int. J. Anal. Appl.*, **22** (2024), 217. https://doi.org/10.28924/2291-8639-22-2024-217
7. S. Vaidyanathan, A. T. Azar, A novel 4-D four-wing chaotic system with four quadratic nonlinearities and its synchronization via adaptive control method, In: *Advances in chaos theory and intelligent control*, Cham: Springer, 2016, 203–224. https://doi.org/10.1007/978-3-319-30340-6_9
8. S. E. Saadi, K. Behih, Z. Bouchama, N. Essounbouli, K. Zehar, Synchronization of chaotic oscillator systems based on adaptive synergetic control theory, *South Florida Journal of Development*, **5** (2024), e4352. https://doi.org/10.46932/sfjdv5n9-014
9. H. X. Cheng, H. H. Li, J. F. Liang, Q. L. Dai, J. Z. Yang, Generalized synchronization between two distinct chaotic systems through deep reinforcement learning, *Chaos Soliton. Fract.*, **199** (2025), 116727. https://doi.org/10.1016/j.chaos.2025.116727
10. Z. Wang, C. Volos, S. T. Kingni, A. T. Azar, V.-T. Pham, Four-wing attractors in a novel chaotic system with hyperbolic sine nonlinearity, *Optik*, **131** (2017), 1071–1078. https://doi.org/10.1016/j.ijleo.2016.12.016
11. F. Zouad, K. Kemih, H. Hamiche, A new secure communication scheme using fractional order delayed chaotic system: design and electronics circuit simulation, *Analog Integr. Circ. Sig. Process.*, **99** (2019), 619–632. https://doi.org/10.1007/s10470-018-01382-x
12. K. S. Oyeleke, K. S. Ojo, A. E. Adeniji, V. T. Odumuyiwa, Simulation of a secure communication scheme via hybrid synchronization of chaotic systems with minimal continuous chaos, *FUDMA Journal of Sciences*, **9** (2025), 38–44.
13. K. Benkouider, A. Sambas, I. M. Sulaiman, M. Mamat, K. S. Nisar, Secure communication scheme based on a new hyperchaotic system, CMC-*Comput. Mater. Con.*, **73** (2022), 1019–1035. https://doi.org/10.32604/cmc.2022.025836
14. B. Wang, X. C. Dong, Secure communication based on a hyperchaotic system with disturbances, *Math. Probl. Eng.*, **2015** (2015), 616137. https://doi.org/10.1155/2015/616137

15. S. Gao, H. H.-C. Iu, U. Erkan, C. Simsek, A. Toktas, Y. H. Cao, A 3D memristive cubic map with dual discrete memristors: design, implementation, and application in image encryption, *IEEE T. Circ. Syst. Vid.*, **35** (2025), 7706–7718. https://doi.org/10.1109/TCSVT.2025.3545868
16. S. Gao, R. Wu, H. H.-C. Iu, U. Erkan, Y. H. Cao, Q. Li, et al., Chaos-based video encryption techniques: A review, *Comput. Sci. Rev.*, **58** (2025), 100816. https://doi.org/10.1016/j.cosrev.2025.100816
17. S. Gao, Z. Y. Zhang, Q. Li, S. Q. Ding, H. H.-C. Iu, Y. H. Cao, Encrypt a story: A video segment encryption method based on the discrete sinusoidal memristive Rulkov neuron, *IEEE T. Depend. Secure*, **22** (2025), 8011–8024. https://doi.org/10.1109/TDSC.2025.3603570
18. S. Gao, R. Wu, X. Y. Wang, J. F. Liu, Q. Li, C. P. Wang, Asynchronous updating Boolean network encryption algorithm, *IEEE T. Circ. Syst. Vid.*, **33** (2023), 4388–4400. https://doi.org/10.1109/TCSVT.2023.3237136
19. U. Erkan, F. Toktas, A. Toktas, Q. Lai, S. Zhou, Y. T. Lin, et al., Multi-layer and multi-directional image encryption algorithm based on hyperchaotic 3D Xin-She Yang map, *Expert Syst. Appl.*, **304** (2025), 130808. https://doi.org/10.1016/j.eswa.2025.130808
20. K. Benkouider, S. Vaidyanathan, A. Sambas, E. Tlelo-Cuautle, A. A. A. El-Latif, B. Abd-El-Atty, A new 5-D multistable hyperchaotic system with three positive Lyapunov exponents: bifurcation analysis, circuit design, FPGA realization and image encryption, *IEEE Access*, **10** (2022), 90111–90132. https://doi.org/10.1109/ACCESS.2022.3197790
21. S. Hussain, Z. Bashir, M. G. A. Malik, Chaos analysis of nonlinear variable order fractional hyperchaotic Chen system utilizing radial basis function neural network, *Cogn. Neurodyn.*, **18** (2024), 2831–2855. https://doi.org/10.1007/s11571-024-10118-9
22. A. Alkhayyat, M. Ahmad, N. Tsafack, M. Tanveer, D. H. Jiang, A. A. Abd El-Latif, A novel 4D hyperchaotic system assisted Josephus permutation for secure substitution-box generation, *J. Sign. Process. Syst.*, **94** (2022), 315–328. https://doi.org/10.1007/s11265-022-01744-9
23. M. Messadi, A. Mellit, K. Kemih, M. Ghanes, Predictive control of a chaotic permanent magnet synchronous generator in a wind turbine system, *Chinese Phys. B*, **24** (2015), 010502. https://doi.org/10.1088/1674-1056/24/1/010502
24. A. Boukabou, A. Chebbah, N. Mansouri, Predictive control of continuous chaotic systems, *Int. J. Bifurcat. Chaos*, **18** (2008), 587–592. https://doi.org/10.1142/S0218127408020501